



Cite this: *Dalton Trans.*, 2025, **54**, 11232

# 1D polymeric and 2D layered zinc monoalkyl phosphates bearing long alkyl chains: synthesis, structural transformations and thermal behaviour†

Harsha Arya  and Ramaswamy Murugavel  \*

The reactivity of two different alkyl phosphate esters with zinc metal ions has been explored. The reaction of zinc nitrate with *n*-octyl phosphate leads to a mixture of  $[(^n\text{OctO})\text{PO}_3\text{Zn}(\text{DMF})]_n$  (**1**) and  $[(^n\text{OctO})\text{PO}_3\text{Zn}(\text{H}_2\text{O})]_n$  (**2a**); similarly, the reaction of zinc nitrate with *n*-hexyl phosphate results in a mixture of  $[(^n\text{HexO})\text{PO}_3\text{Zn}(\text{DMF})]_n$  (**3**) and  $[(^n\text{HexO})\text{PO}_3\text{Zn}(\text{H}_2\text{O})]_n$  (**4**). While the DMF-coordinated compounds **1** and **3** are isolated as single crystals, the water-coordinated compounds **2a** and **4** were obtained as polycrystalline samples. Exposure of these mixtures (**1** and **2a** or **3** and **4**) to ambient humid conditions results in the exchange of coordinated DMF molecules by water molecules and the whole mixture transforming into either **2a** or **4**, respectively. The molecular structures of **1** and **3** have been determined by single-crystal X-ray diffraction studies, revealing them to be one-dimensional coordination polymers. The presence of flexible alkyl chains in **2a** and **4** results in structural transformation, where the interlayer distance in **2a** decreases over time under ambient conditions to form **2b**, and it returns to its initial state on heating at 50 °C for 20 hours in a vacuum. DSC studies for **2a** and **4** show two low-enthalpy reversible transitions below room temperature, which could be associated with the 3D organization of alkyl chains in the structure. Thermal decomposition studies reveal that compounds **2a** and **4** can be utilized as a single-source precursor for ceramic materials. The water contact angles for **2a** and **4** are 100.5° and 98.8°, respectively, which fall within the range of hydrophobic materials, indicating the importance of alkyl chains in imparting the hydrophobicity.

Received 1st April 2025,  
Accepted 21st June 2025

DOI: 10.1039/d5dt00783f

rsc.li/dalton

## 1. Introduction

In recent years, there has been a significant surge in investigations on layered materials due to the exceptional physico-chemical properties and versatile applications exhibited by this class of materials.<sup>1,2</sup> These materials are used in various domains, such as catalysis,<sup>3</sup> ion adsorption,<sup>4</sup> electronics,<sup>5</sup> gas sensing,<sup>6</sup> and energy storage.<sup>2,7</sup> Among the broad spectrum of layered materials, layered metal phosphates have garnered attention due to their structural versatility, chemical tunability, and intrinsic stability.<sup>2–4,7,8</sup> Zinc phosphates represent a promising class of material, with applications as non-toxic anticorrosive agents in paints,<sup>9</sup> support for optical materials,<sup>10</sup> dental cement,<sup>11</sup> glasses,<sup>12</sup> ion exchange materials,<sup>13</sup> electrode coatings,<sup>14,15</sup> nonlinear optical devices,<sup>16,17</sup> and therapeutic applications in cancer treatment.<sup>18,19</sup>

Layered zinc phosphates (LZPs), though relatively unexplored, hold significant potential for a variety of applications. Recent studies highlight their utility in emerging areas such as the development of phosphors,<sup>20</sup> metal ion sensing,<sup>21</sup> and proton conduction.<sup>22</sup> LZPs can be obtained either by using amines or N-donor ligands as the structure-directing group<sup>23,24</sup> or by carefully choosing the organophosphate ligand.<sup>25</sup> However, due to the strong interaction between the layers, it is difficult to exfoliate these layers. In recent times, our group has explored the utility of monoalkyl phosphate precursors in the formation of layered metal phosphates.<sup>26,27</sup> However, reports on zinc alkyl phosphates remain limited.<sup>28–30</sup> Notably, the layered zinc ethyl phosphate reported by Clearfield and coworkers exhibits a structure comprising two-dimensional metal–ligand sheets held together by weak van der Waals interlayer interactions.<sup>29</sup> Such weak interactions facilitate exfoliation into single nanosheets,<sup>26</sup> which can be further exploited for various applications.

Alkyl phosphates additionally offer a unique advantage in the synthesis of metal phosphates, as their thermally labile alkyl groups enable the formation of ceramic metal phosphates at relatively low temperatures.<sup>31,32</sup> Over the past few

Department of Chemistry, Indian Institute of Technology Bombay, Powai, Mumbai-400076, India. E-mail: rmv@chem.iitb.ac.in

†Electronic supplementary information (ESI) available. CCDC 2350478 and 2350479. For ESI and crystallographic data in CIF or other electronic format see DOI: <https://doi.org/10.1039/d5dt00783f>

decades, two groups, Murugavel and coworkers and Tilley and coworkers, have shown the utility of di-*tert*-butyl phosphate-based metal complexes as synthons for ceramic metal phosphate synthesis.<sup>33–42</sup> Recently, we started investigating mono-alkyl phosphates for the formation of ceramic phosphates and showed that their exfoliation, followed by thermolysis, yielded metal phosphate materials with enhanced supercapacitance properties.<sup>26,43</sup>

The alkyl chain undergoes deformation with changes in temperature. Presence of longer alkyl chains, in particular, is anticipated to exhibit temperature-dependent structural transitions.<sup>44–48</sup> These transitions find utility in functional applications, including the development of actuators<sup>48</sup> and cobalt-based systems with unique spin-crossover behavior.<sup>49,50</sup> However, crystallization of charge-neutral complexes with extended alkyl chains remains challenging, limiting detailed structural elucidation of these systems. To investigate structural transitions in the alkyl chain-bearing metal phosphates, we previously studied a calcium ethylhexyl phosphate complex,  $[(\text{phen})\text{Ca}(\text{ehpH})_2]_n$ .<sup>51</sup> This compound was crystallized by exploiting the robustness imparted by the N-donor chelating ligand 1,10-phenanthroline,<sup>51</sup> which helped in crystallization and allowed for the observation of a low-temperature structural transformation. However, the rigidity offered by 1,10-phenanthroline also constrained the extent of the structural transition.

Given the above background, in the current study, we have investigated a new family of zinc alkyl phosphates  $[(\text{RO})\text{PO}_3\text{Zn}(\text{solvent})]_n$  (where R = *n*-hexyl or *n*-octyl; solvent = DMF or water), whose R groups are made of highly flexible long alkyl chains, with the objective to realize the full range of structural transitions/transformations that these alkyl chains can undergo under a variety of conditions. The details of this study are presented in the following contribution.

## 2. Experimental section

### 2.1. Materials, methods, and measurements

All the experimental manipulations were carried out under ambient conditions.  $\text{Zn}(\text{NO}_3)_2 \cdot 6\text{H}_2\text{O}$  (Spectrochem) was procured from commercial sources and used as received. Dimethylformamide (DMF) (Finar) was dried over  $\text{CaSO}_4$  and subsequently distilled under reduced pressure and stored over 4 Å molecular sieves. The ligands *n*-hexyl and *n*-octyl phosphates were synthesized by following reported procedures.<sup>52</sup> Melting points were measured in glass capillaries and are reported uncorrected. Fourier transform infrared (FT-IR) spectra were recorded using a PerkinElmer Spectrum One FT-IR spectrometer with diluted samples prepared as KBr discs. Microanalyses were performed on a Vario MICRO cube microanalyzer (Elementar Analysensysteme, Germany). Solid state  $^{31}\text{P}$  CP-MAS NMR (303 MHz) studies were performed by diluting samples with KBr on a Bruker BioSpin Ascend 750 MHz spectrometer (for 1–4) and solid-state  $^{31}\text{P}$  single-pulse NMR (162 MHz) on a Bruker 400 MHz spectrometer (for

2a–800 °C and 4–800 °C). Powder X-ray diffraction studies were carried out on a Rigaku SmartLab SE diffractometer using  $\text{Cu K}_\alpha$  radiation (1.5419 Å). Variable temperature powder XRD measurements were performed in air using a Rigaku HT 1500 high-temperature attachment, with a heating rate of 10 °C min<sup>−1</sup>. At each measurement temperature, the sample was stabilized for 15 minutes before data collection. Thermogravimetric analyses were performed under a nitrogen gas stream at a heating rate of 10 °C min<sup>−1</sup> using a Rigaku STA8122 TGA system. Contact angle measurements were performed at room temperature on an Acam series Apex goniometer (India). Contact angle measurements of 2a and 4 were carried out in triplicate using pellets made on an FT-IR hydraulic press. A total of 5 µL of water was added on the surface of each pellet, and the average contact angles along with the standard deviation were recorded. Differential scanning calorimetric measurements were performed on a Rigaku DSCvesta calorimeter. An empty aluminium pan was used as a reference. 7.9 mg of 2a and 7.1 mg of 4 were used for carrying out the experiment. The measurements were performed in two cycles to confirm the reproducibility. The data obtained in the second cycle were used to calculate the enthalpy and the position of the transition.

Morphologies were studied using FEG-SEM on a ZEISS Ultra 55 field-emission gun-scanning electron microscope operating at an accelerating voltage of 3 kV. EDS mapping was performed on the same samples but at 18 kV using an in-lens detector. The samples for SEM and EDS measurements were prepared by smearing powders of 2a and 4 on carbon paper, whereas samples of the pyrolyzed products were prepared by drop-casting well-dispersed suspensions (in isopropanol) of 2a–800 °C and 4–800 °C on a silicon substrate. The samples were sputtered with gold before imaging. Raman spectra were recorded on a Witec 300 Micro Raman spectrometer equipped with He–Ne (632.8 nm) laser excitation sources. Inductively coupled plasma-atomic emission spectroscopy (ICP-AES) analyses were carried out on a SPECTRO ARCOS Simultaneous ICP instrument.

### 2.2. Synthesis of $[(^n\text{OctO})\text{PO}_3\text{Zn}(\text{DMF})]_n$ (1) and $[(^n\text{OctO})\text{PO}_3\text{Zn}(\text{H}_2\text{O})]_n$ (2a and 2b)

A solution of *n*-octyl phosphate (0.5 mmol, 105 mg) in DMF (10 mL) was added to a solution of  $\text{Zn}(\text{NO}_3)_2 \cdot 6\text{H}_2\text{O}$  (0.5 mmol, 148.5 mg) in DMF (10 mL) under constant stirring. The resulting clear solution was allowed to evaporate at room temperature to obtain white plate-like crystals of 1 along with a white precipitate of 2a, after two weeks. Single crystals of 1 were separated manually under an optical microscope.

**Compound 1.** Yield: 30 mg (19%); Mp. >300 °C; elem. anal. found (calcd) (%) for  $\text{C}_{11}\text{H}_{24}\text{NO}_5\text{PZn}$  ( $M_r = 346.67$ ): C: 37.25 (38.11), H: 6.5 (6.98), N: 3.64 (4.04); FT-IR (KBr pellet, cm<sup>−1</sup>): 1120 (s), 1085 (s), 1207 (w), 1386 (w), 1657 (s), 2852 (w), 2925 (m), 2958 (m), 3431 (w), 3562 (w);  $^{31}\text{P}$  NMR (CP-MAS, 303 MHz):  $\delta$  4.25 ppm; TGA: temp range °C (% weight loss): 80–160 (observed: 21; calculated: 21, DMF), 260–320 (observed: 35; calculated: 35, octene; 0.5 H<sub>2</sub>O). *Note:* the discrepancy

observed in the elemental analysis values is due to its dynamic conversion to **2** through DMF–H<sub>2</sub>O exchange.

**Compound 2a.** Yield: 47 mg (32%); Mp. >300 °C; elem. anal. found (calcd) (%) for C<sub>8</sub>H<sub>19</sub>O<sub>5</sub>PZn (*M<sub>r</sub>* = 291.6): C: 32.85 (32.95), H: 6.35 (6.57). FT-IR (KBr pellet, cm<sup>−1</sup>): 1060 (s), 1113 (s), 1453 (w), 1634 (w), 2859 (w), 2930 (m), 2958 (m), 3431 (w), 3562 (w). <sup>31</sup>P NMR (CP-MAS, 303 MHz): δ 5.75 ppm. TGA: temp range °C (% weight loss): 122–207 (observed: 5; calculated: 6, H<sub>2</sub>O), 207–304 (observed: 42; calculated: 41, octene; 0.5 H<sub>2</sub>O).

**In situ conversion of 1 into 2b.** On removing crystals of **1** from the reaction mixture and exposing them to an open atmosphere under ambient conditions, DMF molecules in **1** exchange with atmospheric water to form **2a**, which eventually transforms to **2b**.

**Compound 2b (formed by in situ conversion of 1 into 2b).** Yield: 30 mg (2%); Mp. >300 °C; elem. anal. found (calcd) (%) for C<sub>8</sub>H<sub>19</sub>O<sub>5</sub>PZn (*M<sub>r</sub>* = 291.6): C: 33.27 (32.95), H: 6.58 (6.57); FT-IR (KBr pellet, cm<sup>−1</sup>): 1015 (s), 1028 (s), 1062 (s), 1085 (s), 1113 (s), 1262 (w), 1466 (w), 1631 (w), 2358 (w), 2855 (w), 2927 (m), 2955 (m), 3356 (w); <sup>31</sup>P NMR (CP-MAS, 303 MHz): δ 5.17 ppm.

### 2.3. Synthesis of [(<sup>n</sup>HexO)PO<sub>3</sub>Zn(DMF)]<sub>n</sub> (**3**) and [(<sup>n</sup>HexO)PO<sub>3</sub>Zn(H<sub>2</sub>O)]<sub>n</sub> (**4**)

Compounds **3** and **4** were prepared by following a procedure similar to that for **1** and **2** using *n*-hexyl phosphate (0.5 mmol, 91 mg) and an equimolar amount of zinc nitrate.

**Compound 3.** Yield: 4 mg (2.5%); Mp. >300 °C; elem. anal. found (calcd) (%) for C<sub>9</sub>H<sub>20</sub>NO<sub>5</sub>PZn (*M<sub>r</sub>* = 318.6): C: 32.68 (32.31), H: 6.82 (6.02), N: 2.78 (4.19); FT-IR (KBr pellet, cm<sup>−1</sup>): 1117 (s), 1077 (s), 1200 (w), 1390 (w), 1664 (s), 2861 (w), 2930 (m), 2958 (m), 3431 (w); <sup>31</sup>P NMR (CP-MAS, 303 MHz): δ 0.42 ppm, δ 3.62 ppm; TGA: temp range °C (% weight loss): 40–160 (observed: 24.3; calculated: 23, DMF), 260–306 (observed: 29; calculated: 29, hexene; 0.5 H<sub>2</sub>O). *Note:* the discrepancy observed in the elemental analysis values is due to its dynamic conversion to **4** through DMF–H<sub>2</sub>O exchange.

**Compound 4.** Yield: 75 mg (57%); Mp. >300 °C; elem. anal. found (calcd) (%) C<sub>6</sub>H<sub>15</sub>O<sub>5</sub>PZn (*M<sub>r</sub>* = 263.5): C: 27.88 (27.35), H: 5.70 (5.74). FT-IR (KBr pellet, cm<sup>−1</sup>): 1060 (s), 1113 (s), 1453 (w), 1634 (w), 2859 (w), 2930 (m), 2958 (m), 3431 (w), 3562 (w); <sup>31</sup>P NMR (CP-MAS, 303 MHz): δ 3.47 ppm; TGA: temp range °C (% weight loss): 122–207 (observed: 7; calculated: 7, H<sub>2</sub>O), 207–304 (observed: 37; calculated: 35, hexene; 0.5 H<sub>2</sub>O).

**Compound 4 (formed by in situ conversion of 3 into 4).** Yield: 4 mg (2.5%); Mp. >300 °C; elem. anal. found (calcd) (%) C<sub>6</sub>H<sub>15</sub>O<sub>5</sub>PZn (*M<sub>r</sub>* = 263.5): C: 27.09 (27.35), H: 5.73 (5.74); FT-IR (KBr pellet, cm<sup>−1</sup>): 550 (w), 854 (w), 1015 (s), 1028 (s), 1062 (s), 1085 (s), 1113 (s), 1384 (w), 1467 (w), 1631 (w), 2358 (w), 2855 (w), 2956 (m), 2955 (m), 3356 (w); <sup>31</sup>P NMR (CP-MAS, 303 MHz): δ 3.84 ppm.

### 2.4. Reversibility of DMF–water exchange in **2a** and **4**

20 mg of **2a** was suspended in 10 mL of DMF in a 20 mL glass vial and sonicated under heated conditions (50 °C) for 2 hours. Following sonication, the solid was filtered from the

suspension and immediately analyzed by powder XRD. To further assess the reversibility of the solvent exchange, the same sample was treated with a drop of deionized water, dried, and subjected to powder XRD analysis once again.

Similarly, 20 mg of compound **4** was suspended in 10 mL of DMF in a 20 mL glass vial and sonicated at 50 °C for 2 hours. However, in this case, no conversion to DMF-exchanged species was observed as seen by powder XRD. Hence, the next step was not performed.

### 2.5. Reversibility of **2a** to **2b** phase change

30 mg of **2b** was heated under vacuum at 50 °C for 20 hours, followed by immediate analysis using PXRD and TGA.

### 2.6. Solid state thermolysis

Compound **2a** (84 mg) was placed in an alumina crucible and heated to 800 °C in air at a heating rate of 10 °C min<sup>−1</sup> for 24 h followed by cooling the sample to room temperature, yielding crystalline **2a**–800 °C. Yield: 31 mg (72%); FT-IR (KBr pellet, cm<sup>−1</sup>): 1129 (s), 1101 (m), 1078 (m), 1044 (m), 1014 (m), 946 (s), 758 (s), 646 (w), 543 (s); ICP-AES: Zn : P ratio: 1 : 0.915.

Similarly, compound **4** (81 mg) was pyrolyzed at 800 °C to obtain **4**–800 °C. Yield: 38 mg (81%); FT-IR (KBr pellet, cm<sup>−1</sup>): 1122 (s), 1101 (m), 1080 (m), 1051 (m), 1014 (m), 958 (s), 753 (s), 640 (w), 543 (s). ICP-AES: Zn : P ratio: 1 : 1.32.

### 2.7. Single-crystal X-ray diffraction studies

Single crystals of compounds **1** and **3** suitable for X-ray diffraction analysis were grown from the reaction mixture and mounted on a BRUKER D8 QUEST diffractometer equipped with an IμS DIAMOND microfocus Mo-K<sub>α</sub> radiation source (λ = 0.71073 Å). Data collection, data integration, and indexing were performed with the CrysAlisPro software suite.<sup>53</sup> The structures were solved using the SHELXT program and refined with SHELXL<sup>54</sup> by the least squares method using the Olex2 package.<sup>55</sup> The data collection and refinement processes are summarized in Table 1. CCDC deposition numbers 2350478 and 2350479† for **1** and **3** contain the supplementary crystallographic data for this paper, which can be obtained free of charge from the Cambridge Crystallographic Data Centre.

## 3. Results and discussion

### 3.1. Synthesis and characterization of zinc alkyl phosphates

The reaction of equimolar quantities of zinc nitrate hexahydrate and *n*-octyl phosphate (**L1**) in DMF leads to the formation of a DMF-coordinated polymer [(<sup>n</sup>OctO)PO<sub>3</sub>Zn(DMF)]<sub>n</sub> (**1**) as the minor product, and a water-coordinated polymer [(<sup>n</sup>OctO)PO<sub>3</sub>Zn(H<sub>2</sub>O)]<sub>n</sub> (**2a**) as the major product. Exposing crystals of **1** to air results in rapid exchange of DMF molecules with moisture (H<sub>2</sub>O), leading to its conversion to **2a** (Scheme 1). Similarly, [(<sup>n</sup>HexO)PO<sub>3</sub>Zn(DMF)]<sub>n</sub> (**3**) and [(<sup>n</sup>HexO)PO<sub>3</sub>Zn(H<sub>2</sub>O)]<sub>n</sub> (**4**) were synthesized using *n*-hexyl phosphate (**L2**). These reactions were repeated multiple times under identical conditions, consistently yielding the same products,

**Table 1** Crystallographic data for  $[(n\text{-OctO})\text{PO}_3\text{Zn}(\text{DMF})]_n$  (**1**) and  $[(n\text{-HexO})\text{PO}_3\text{Zn}(\text{DMF})]_n$  (**3**)

Compound number	<b>1</b>	<b>3</b>
Sample code	RM-HA-62	RM-HA-61
Empirical formula	$\text{C}_{11}\text{H}_{24}\text{NO}_5\text{PZn}$	$\text{C}_9\text{H}_{20}\text{NO}_5\text{PZn}$
Formula weight	346.65	318.60
Temperature/K	150.0(1)	107.0(4)
Crystal system	Triclinic	Triclinic
Space group	$P\bar{1}$	$P\bar{1}$
$a/\text{\AA}$	5.4254(2)	5.4197(2)
$b/\text{\AA}$	9.4114(3)	9.3778(4)
$c/\text{\AA}$	15.2643(4)	13.3722(5)
$\alpha/^\circ$	85.187(2)	83.203(3)
$\beta/^\circ$	82.270(2)	88.754(3)
$\gamma/^\circ$	82.405(3)	82.318(3)
Volume/ $\text{\AA}^3$	763.81(4)	668.79(5)
$Z$	2	2
$\rho_{\text{calc}}, \text{g cm}^{-3}$	1.507	1.582
$\mu/\text{mm}^{-1}$	1.726	1.964
$F(000)$	364.0	332.0
Crystal size/ $\text{mm}^3$	$0.62 \times 0.154 \times 0.026$	$0.595 \times 0.103 \times 0.095$
Radiation/ $\text{\AA}$	Mo $K_\alpha$ ( $\lambda = 0.71073$ )	Mo $K_\alpha$ ( $\lambda = 0.71073$ )
$2\theta$ range for data collection/ $^\circ$	4.376 to 50.05	4.412 to 49.996
Index ranges	$-6 \leq h \leq 6, -11 \leq k \leq 11, -18 \leq l \leq 18$	$-6 \leq h \leq 6, -11 \leq k \leq 11, -15 \leq l \leq 15$
Reflections collected	28 102	25 008
Independent reflections	2700 [ $R_{\text{int}} = 0.0531$ , $R_{\text{sigma}} = 0.0234$ ]	2358 [ $R_{\text{int}} = 0.0465$ , $R_{\text{sigma}} = 0.0215$ ]
Data/restraints/parameters	2700/0/175	2358/0/157
Goodness-of-fit on $F^2$	1.033	1.053
Final $R$ indexes [ $I \geq 2\sigma(I)$ ]	$R_1 = 0.0272$ , $wR_2 = 0.0655$	$R_1 = 0.0225$ , $wR_2 = 0.0516$
Final $R$ indexes [all data]	$R_1 = 0.0292$ , $wR_2 = 0.0670$	$R_1 = 0.0235$ , $wR_2 = 0.0521$
Largest diff. peak/hole/ $\text{e \AA}^{-3}$	0.37/−0.43	0.34/−0.34

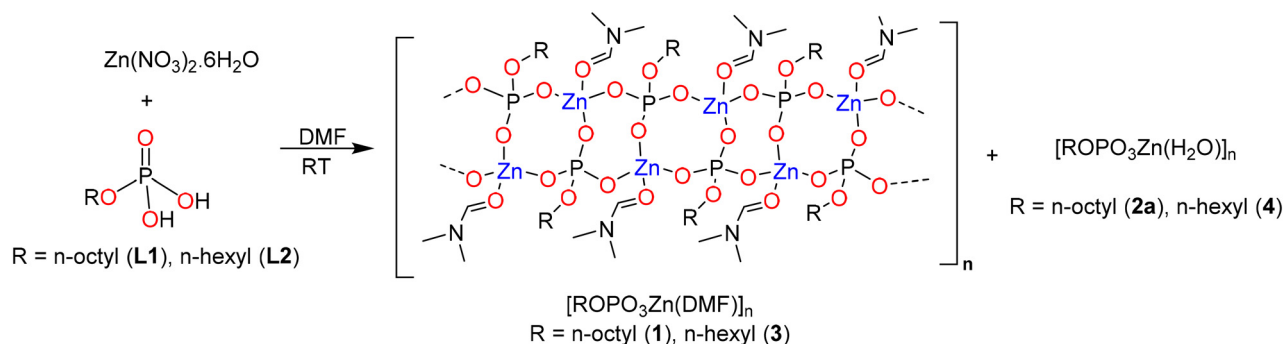
thereby confirming their high reproducibility. These polymers **1–4** were characterized by various spectroscopic and analytical techniques.

The FT-IR spectra of **1–4** show strong absorption bands around  $1150\text{--}1000 \text{ cm}^{-1}$ , corresponding to  $\text{P}=\text{O}$  stretching, and  $\text{M}=\text{O}-\text{P}$  asymmetric and symmetric vibrations (Fig. S1 and S2†).<sup>26,35</sup> The absorption bands observed at 2917 and

$2836 \text{ cm}^{-1}$  correspond to C–H stretching of the alkyl groups. The elemental analysis values obtained for **2a** and **4** match well with the calculated values. However, the values for both **1** and **3** show a discrepancy between the observed and calculated elemental analysis values due to their tendency to rapidly undergo interconversion to **2a** and **4**, respectively. The  $^{31}\text{P}$  CP-MAS NMR spectra of **1** and **3** exhibit broad peaks due to the dynamic exchange of DMF with moisture, which converges to a single peak at  $\delta$  5.75 and 3.47 ppm for **2a** and **4**, respectively (Fig. 1 and S3†). The additional minor signal observed at  $\delta$  7.87 ppm for **4** can be attributed to the presence of minor species of a slightly different environment around the phosphorus centre, probably due to a different conformation of alkyl chains. However, we have not been able to determine conclusively the exact source of this signal.

### 3.2. Crystal structure of 1D coordination polymers **1** and **3**

Colourless plate-shaped crystals of **1** and **3** were obtained from the reaction mixture after two weeks at room temperature. X-ray diffraction studies reveal that compounds **1** and **3** crystallize in the triclinic  $P\bar{1}$  space group and are isostructural. The asymmetric part of the unit cell of **1** and **3** consists of one zinc ion, one alkyl phosphate anion ( $\text{ROPO}_3^{2-}$ ,  $\text{R} = n\text{-octyl}$  (**1**) and  $n\text{-hexyl}$  (**3**)) and one coordinated DMF molecule. The zinc ion is coordinated with three oxygen atoms of different alkyl phosphate ligands, while the fourth coordination site is occupied by the oxygen atom of the DMF molecule (Fig. 2a and b). This arrangement results in distorted tetrahedral geometry around the zinc ion with  $\text{Zn}-\text{O}(\text{P})$  bond lengths of 1.925(2)  $\text{\AA}$  for  $\text{Zn1}-\text{O3}^1$ , 1.910(2)  $\text{\AA}$  for  $\text{Zn1}-\text{O2}$ , and 1.914(2)  $\text{\AA}$  for  $\text{Zn1}-\text{O1}^2$  in **1**, and 1.928(1)  $\text{\AA}$  for  $\text{Zn1}-\text{O3}^1$ , 1.912(1)  $\text{\AA}$  for  $\text{Zn1}-\text{O2}$ , and 1.913(1)  $\text{\AA}$  for  $\text{Zn1}-\text{O1}^2$  in **3** ( $\#1$ :  $-1 + X, +Y, +Z$ ;  $\#2$ :  $1 - X, 1 - Y, 2 - Z$ ;  $\#3$ :  $1 + X, +Y, +Z$ ). The tetrahedral geometry around the zinc atom has also been confirmed by shape analysis (Tables S1 and S2†).<sup>56</sup> The  $\text{Zn}-\text{O}(\text{P})$  bond lengths in **1** and **3** are comparable to those observed in earlier reported zinc alkyl and aryl phosphates.<sup>29,35,57</sup> The bond length of  $\text{Zn}-\text{O}$  from the DMF molecule is 2.025(2)  $\text{\AA}$  ( $\text{Zn1}-\text{O5}$ ) in **1** and 2.023(1)  $\text{\AA}$  ( $\text{Zn1}-\text{O5}$ ) in **3**, which are significantly longer compared to the  $\text{Zn}-\text{O}(\text{P})$  bonds. The  $\text{O}-\text{Zn}-\text{O}$  bond angles for the distorted tetrahedron range from  $100.00(7)^\circ$  to  $115.69(7)^\circ$  in **1** and  $99.92(6)^\circ$  to

**Scheme 1** Synthesis of zinc phosphates **1–4**.



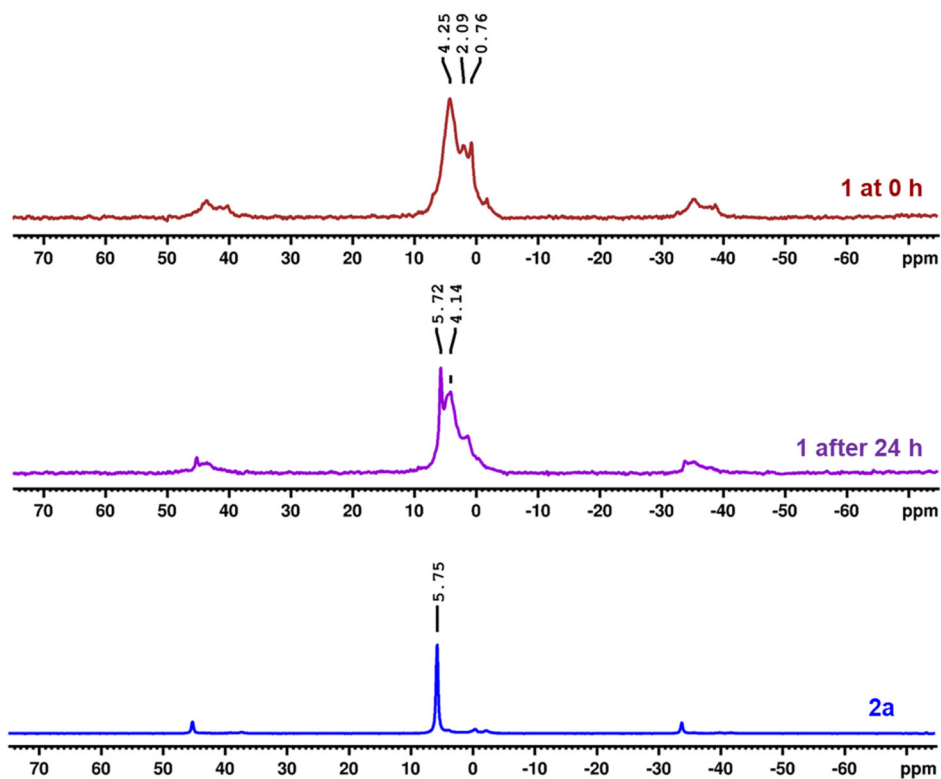


Fig. 1  $^{31}\text{P}$  CP-MAS NMR spectra of **1** and **2a** (303 MHz).

115.83(6) $^\circ$  in **3**, showcasing the extent of distortion around the tetrahedral zinc centres. Similarly, the O–P–O bond angles vary in the range of 102.42(9) $^\circ$ –112.86(9) $^\circ$  for **1** and 102.39(8) $^\circ$ –112.94(8) $^\circ$  for **3**. The observed P–O bond lengths in **1** are P1–O1: 1.505(2), P1–O2: 1.522(2), P1–O3: 1.521(2), and P1–O4: 1.594(2) Å; similar distances were observed in **3**: P1–O1: 1.510(1), P1–O2: 1.526(1), P1–O3: 1.521(2), and P1–O4: 1.595(1) Å. The selected bond angles and bond lengths for **1** and **3** have been listed in Tables S3 and S4.<sup>†</sup>

Alkyl phosphate ligands in compounds **1** and **3** are tridentate and exhibit a [3.111] mode of coordination (Fig. 2c and d).<sup>26,58</sup> It should be noted that the three ligating oxygen atoms bind three different zinc ions. In other words, the zinc ions are ligated/bridged by three different phosphate oxygen atoms arising from three different phosphate ligands. This leads to the formation of  $\text{Zn}_2\text{O}_4\text{P}_2$  eight-membered rings, which resemble the Single-4-Ring (S4R) zeolitic SBUs (Fig. S4a and S5a<sup>†</sup>). Moreover, the side-by-side fusion of these S4R rings leads to the formation of 1D polymeric chains whose central core resembles a ‘tape’ made up of indefinite edge-sharing S4R rings extending along the *a*-axis in both **1** and **3** (Fig. 2c and d). In the 1D polymeric chain, the eight-membered rings of the adjacent S4R rings exhibit different ring conformations, as evidenced by different Zn–Zn diagonal distances. These distances are 4.2278(4) and 4.5003(4) Å for adjacent rings in **1** (Fig. S4b<sup>†</sup>), and 4.2306(4) and 4.4959(4) Å in **3** (Fig. S5b<sup>†</sup>). The inorganic tape is capped on both sides by the coordinated

DMF molecules on zinc and the long alkoxy chain on phosphorus. The presence of all *trans* octyloxy and hexyloxy chains (which do not coil around), leads to the stacking of these 1D tape-like polymers adjacent to each other in the crystal lattice (Fig. 3).

The presence of hydrophobic van der Waals type interactions between the alkoxy groups of the immediate neighbours in these complexes leads to a packing arrangement such as that shown in Fig. 3a and b, where the alkoxy chains of the adjacent polymeric chains are involved in near-perfect interdigitation, as has been normally observed in many other layered metal alkyl phosphates and phosphonates,<sup>26,29</sup> albeit in the present case, the crystal packing is due to agglomeration of polymeric chains and not 2D sheets. The packing diagrams of **1** and **3** further reveal that owing to perfect interdigitation, they achieve close packing, exhibiting inter-polymer distances of 15.3 Å in **1** and 13.4 Å in **3**. Clearfield and co-workers reported water-coordinated zinc ethyl phosphate that adopts a two-dimensional polymeric structure.<sup>29</sup> Similarly, the long-chain phosphonate analogue, calcium hexyl phosphonate, reported by Mallouk also forms a two-dimensional polymeric network.<sup>59</sup> These studies suggest that both short- and long-chain alkyl phosphonates and phosphates tend to favor the formation of two-dimensional polymeric architectures. However, in the case of **1** and **3**, where DMF is coordinated to the metal centre, the relatively larger steric bulk hinders the growth of the polymer in the perpendicular direction. As a

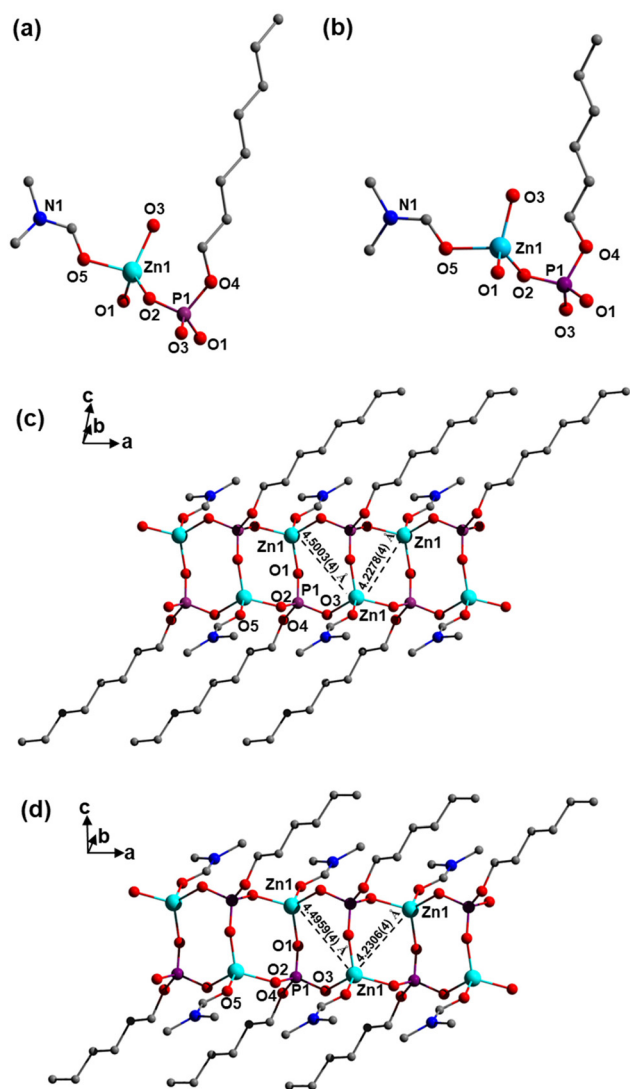


**Fig. 2** (a and b) Molecular structure of  $[(^n\text{OctO})\text{PO}_3\text{Zn}(\text{DMF})]_n$  (**1**) and  $[(^n\text{HexO})\text{PO}_3\text{Zn}(\text{DMF})]_n$  (**3**) showing the section of the polymeric structure and geometry around the zinc atom (asymmetric unit). (c and d) Edge sharing S4R rings forming a 1D coordination polymer for **1** and **3**, respectively (hydrogen atoms are omitted for clarity; colour scheme;  $\text{Zn}$ : cyan,  $\text{P}$ : purple,  $\text{O}$ : red,  $\text{N}$ : blue,  $\text{C}$ : grey).

result, one-dimensional DMF-coordinated polymers **1** and **3** were isolated instead.

### 3.3. Structural evolution by exchange of DMF with water molecules

Although 1D polymers **1** and **3** have been isolated as single crystals and their structures determined by SCXRD, both solids are relatively unstable in open air and readily convert into their secondary polymeric forms **2a** and **4**, respectively. While the presence of bulky DMF at the fourth coordination site on the zinc ion in **1** and **3** ensures the isolation of 1D polymers, the rapid replacement of DMF by water on standing over a period of time brings about interesting changes in the PXRD pattern. The most intriguing aspect of the structures of **1** and

**3** emerges from closer examination of the PXRD patterns of their freshly prepared samples. The powder XRD pattern of **1** shows slight deviations from the simulated pattern obtained from the single-crystal structure (Fig. 4a and S6†). The slight deviations can be attributed to crystal morphology and temperature-dependent changes in the orientation of the alkyl chains. This is because powder XRD patterns were recorded at room temperature, whereas the molecular structure studies were conducted at 150 K and 107 K for **1** and **3**, respectively.<sup>51</sup> Thus, as has been mentioned above, compound **1** is sufficiently stable for its PXRD pattern to be recorded for its pure form obtained from the single crystals isolated freshly from the mother liquor. However, the PXRD pattern for a similar sample of **3** is entirely different (Fig. 4a and S7†), where one observes additional stronger reflections of compound **4**, with only a minor proportion of **3**.

The powder XRD pattern of **2a** exhibits reflections at  $2\theta$  values of  $3.7^\circ$  ( $d = 23.8 \text{ \AA}$ ),  $7.4^\circ$  ( $d = 11.9 \text{ \AA}$ ), and  $11.2^\circ$  ( $d = 7.9 \text{ \AA}$ ) (Fig. 4a). Likewise, the powder XRD pattern of **4** shows reflections at  $2\theta = 4.5^\circ$  ( $d = 19.5 \text{ \AA}$ ),  $9.0^\circ$  ( $d = 9.8 \text{ \AA}$ ), and  $13.5^\circ$  ( $d = 6.5 \text{ \AA}$ ) (Fig. 4a), indicating a layered structure. The lowest angle of reflection has the highest intensity, and this progressively decreases moving towards the higher angles of reflection. Furthermore, the observed  $d$ -spacings follow a 1 : 1/2 : 1/3 ratio, suggesting a highly organized layered structure exhibiting reflections corresponding to the 001, 002, and 003 planes.<sup>60–62</sup> In case of **2a**, the interlayer distance has increased to a higher value ( $d = 23.8 \text{ \AA}$ ) than that seen for the interdigitated polymer **1** ( $15.3 \text{ \AA}$ ). Similarly, in the case of **4**, the interlayer distance has increased to a higher value ( $d = 19.6 \text{ \AA}$ ) compared to that observed in the interdigitated 1D polymer **3** ( $13.4 \text{ \AA}$ ). This difference can be explained by the opening up of interdigitated alkyl chains on exchange of DMF with  $\text{H}_2\text{O}$  (Fig. 3a and b) to form 2D layered materials. A similar kind of expanded structure for aluminium alkyl phosphates and calcium hexyl phosphonates has been previously observed by the groups of Tanaka<sup>60–62</sup> and Mallouk.<sup>59</sup> The interlayer distance in metal alkyl phosphates and phosphonates increases with an increase in the number of carbon atoms in the alkyl chain.<sup>60–63</sup> Interlayer distances reported for water-coordinated zinc methyl phosphonate and zinc ethyl phosphonate are  $8.73 \text{ \AA}$  and  $10.14 \text{ \AA}$ , respectively.<sup>64</sup> Similarly, water-coordinated zinc ethyl phosphate shows an interlayer spacing of  $10.2 \text{ \AA}$ .<sup>29</sup> In this study, when the alkyl chain length increases to six and eight carbon atoms, the interlayer spacing expands significantly to  $19.5 \text{ \AA}$  and  $23.8 \text{ \AA}$ , respectively.

Additionally, SEM analysis was performed to study the morphological features of polymers **1–4** (Fig. 4b, c and S8†). The SEM image of **1** shows a spindle formed by a collection of rod-shaped microcrystals. The SEM images of **4** reveal sheets cleanly stacked one over the other to form a lamellar compound, indicating the significance of alkyl groups for synthesizing compounds having layered morphology.

### 3.4. Tracking of DMF–water exchange by PXRD studies

The powder XRD patterns recorded after ambient drying of **1** and **3** did not match their respective simulated patterns but

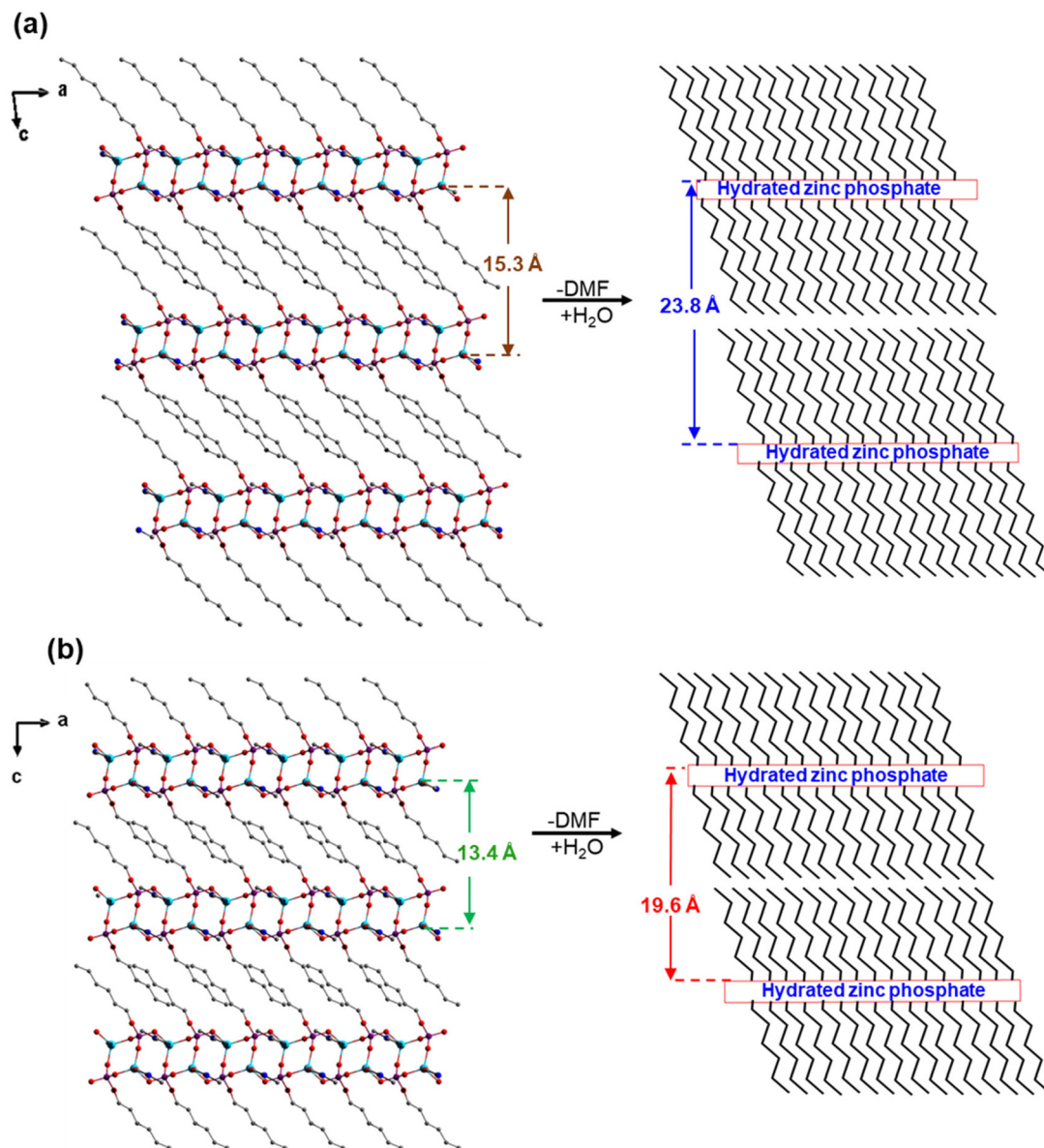


**Fig. 3** (a) Variation in the interlayer distance of interdigitated 1D polymer  $[(l''\text{OctO})\text{PO}_3\text{Zn}(\text{DMF})]_n$  (**1**), upon transformation to  $[(l''\text{OctO})\text{PO}_3\text{Zn}(\text{H}_2\text{O})]_n$  (**2a**). (b) Variation in interlayer distance upon the transformation of  $[(l''\text{HexO})\text{PO}_3\text{Zn}(\text{DMF})]_n$  (**3**) to  $[(l''\text{HexO})\text{PO}_3\text{Zn}(\text{H}_2\text{O})]_n$  (**4**), showing the expansion of the interlayer distance on coordination with water [colour scheme;  $\text{Zn}$ :  $\text{Zn}$ ,  $\text{P}$ :  $\text{P}$ ,  $\text{O}$ :  $\text{O}$ ,  $\text{N}$ :  $\text{N}$ ,  $\text{C}$ :  $\text{C}$ ].

instead closely matched the diffraction patterns recorded for **2a** and **4**, respectively. Time-dependent powder XRD studies were therefore conducted over a period of time to investigate the structural evolution of **2a** from **1** and **4** from **3**, respectively. The powder XRD patterns were recorded at various intervals after removing crystals of **1** and **3** from the reaction mixture (Fig. 5 and S9†). Initially, a fresh sample of **1** shows an XRD pattern corresponding to **1** with a 001 reflection at  $5.6^\circ$  (Fig. 5, 0 h). After two hours, a new pattern emerged featuring reflections at  $3.7^\circ$ ,  $7.4^\circ$ , and  $11.1^\circ$ , indicating the formation of compound **2a**. After eight hours, the majority of compound **1** transforms into **2a**. A similar observation was reported by Kanoh and co-workers., where a 1D polymer transitioned into a 2D

polymer by the loss of coordinated solvent molecules.<sup>65</sup> Given that alkyl phosphates have a propensity to form 2D polymers,<sup>26,29</sup> the alteration in the powder XRD pattern suggested the conversion of 1D polymer **1** into a 2D polymer **2a**. Furthermore, elemental analysis was carried out to verify the exchange of DMF with water, which reveals that the sample is free from nitrogen (of DMF) after 8 hours and correspond to the molecular formula  $[(l''\text{OctO})\text{PO}_3\text{Zn}(\text{H}_2\text{O})]_n$ .

Similarly, fresh crystals of **3** exhibit reflection at  $6.3^\circ$ , which is characteristic to **3**, along with reflections at  $4.5^\circ$ ,  $9.0^\circ$ , and  $13.6^\circ$  that correspond to **4** (Fig. S9†). Reflections corresponding to **4** are dominant, indicating that a significant portion of **3** has already converted into **4** upon removal from

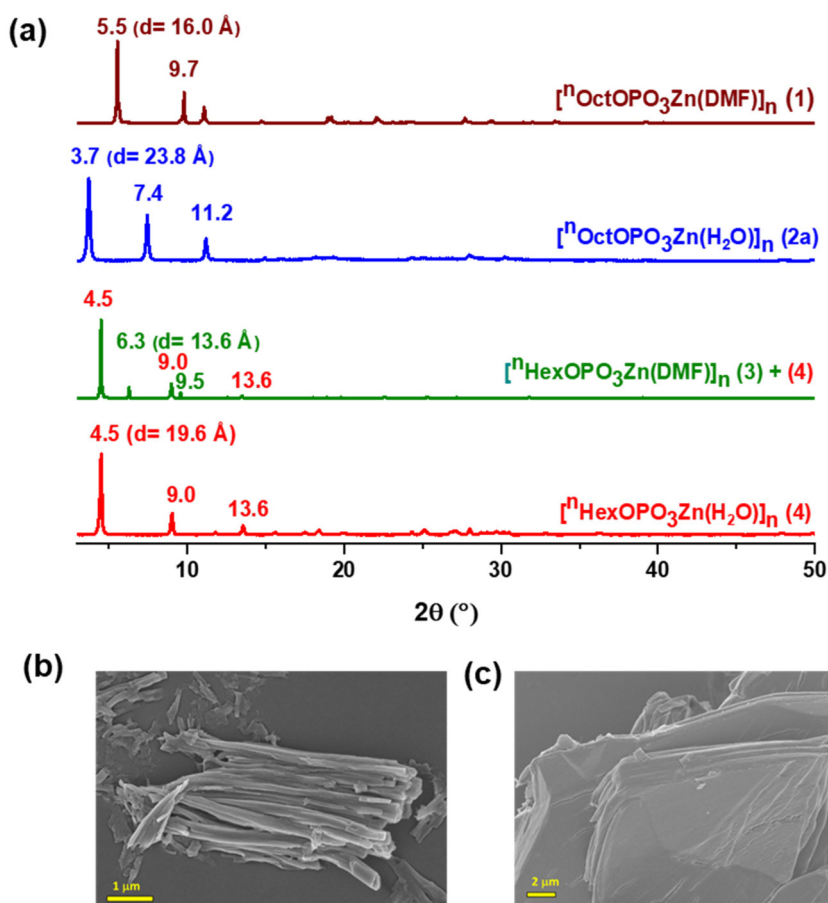


Fig. 4 (a) Powder XRD patterns for 1–4; the interdigitated 1D polymer 1 and 3 shows narrower interlayer spacing compared to 2a and 4, respectively; a pure experimental PXRD pattern for 3 could not be obtained due to rapid solvent exchange. (b and c) SEM images of 1 and 4, respectively.

the solution. The time-dependent powder XRD measurements show that after forty hours, 3 completely transforms into 4. The elemental analysis of the sample of 3 that has completely transformed into 4 matches well with  $[\text{HexO}]\text{PO}_3\text{Zn}(\text{H}_2\text{O})_n$ .

To further confirm DMF–water exchange,  $^{31}\text{P}$  CP-MAS NMR studies were carried out on the solid samples of 1 and 3. The first set of NMR measurements was performed on a fresh batch of crystals immediately after their removal from solution. Subsequently, another set of measurements was performed after allowing the crystals to remain in air. It was observed that the  $^{31}\text{P}$  CP-MAS NMR spectra of the samples immediately removed from solution revealed a broad NMR signal due to the initiation of exchange of DMF with water for both 1 and 3. Upon further exposure to air, distinct resonances corresponding to 2a and 4 began to emerge (Fig. 1 and S3†). To investigate the reversibility of the DMF–water exchange, 2a and 4 were sonicated at  $50^\circ\text{C}$  in DMF for two hours. Powder X-ray diffraction (PXRD) patterns recorded immediately after removing 2a from the suspension showed the appearance of a reflection at  $5.5^\circ$ , characteristic of compound 1, along with reflections corresponding to 2a (Fig. S10†). Furthermore, one drop of water was added to the same sample, which led to the disappearance of the reflection due to 1. This indicates that

the transformation from 1 to 2a via DMF–water exchange is a reversible process. However, subjecting 4 to similar conditions did not result in the regeneration of 3 as seen from its powder XRD plot after sonication in DMF for 2 h under the same conditions (Fig. S11†), suggesting that the DMF–water exchange is either not reversible in this case or that any formation of 3 rapidly reverts back to 4 upon removal from solution.

A second dynamic process sets in for a sample of 2a (obtained by *in situ* conversion from 1) kept under ambient conditions beyond 8 hours (Fig. 5). The PXRD patterns recorded after 15 hours and 21 hours reveal the emergence of a new phase 2b with small shifts in  $2\theta$  values from  $3.7^\circ$  to  $4.1^\circ$ ,  $7.4^\circ$  to  $8.2^\circ$ , and  $11.2^\circ$  to  $12.3^\circ$  (Fig. 5). This dynamic process is complete after approximately two weeks. During the conversion of 2a to 2b, the interlayer spacing marginally decreases from  $23.8 \text{ \AA}$  to  $21.6 \text{ \AA}$ , which can be attributed to the flexibility in the structure due to ordering and disordering of alkyl chains.<sup>44</sup> Although the transformation of 2a to 2b was observed within 15 hours when 2a was generated *in situ* from 1, the conversion was significantly slower in the case of microcrystalline 2a obtained directly from the reaction mixture, requiring more than two weeks for complete transformation into 2b. Elemental analysis indicated that 2a and 2b share the



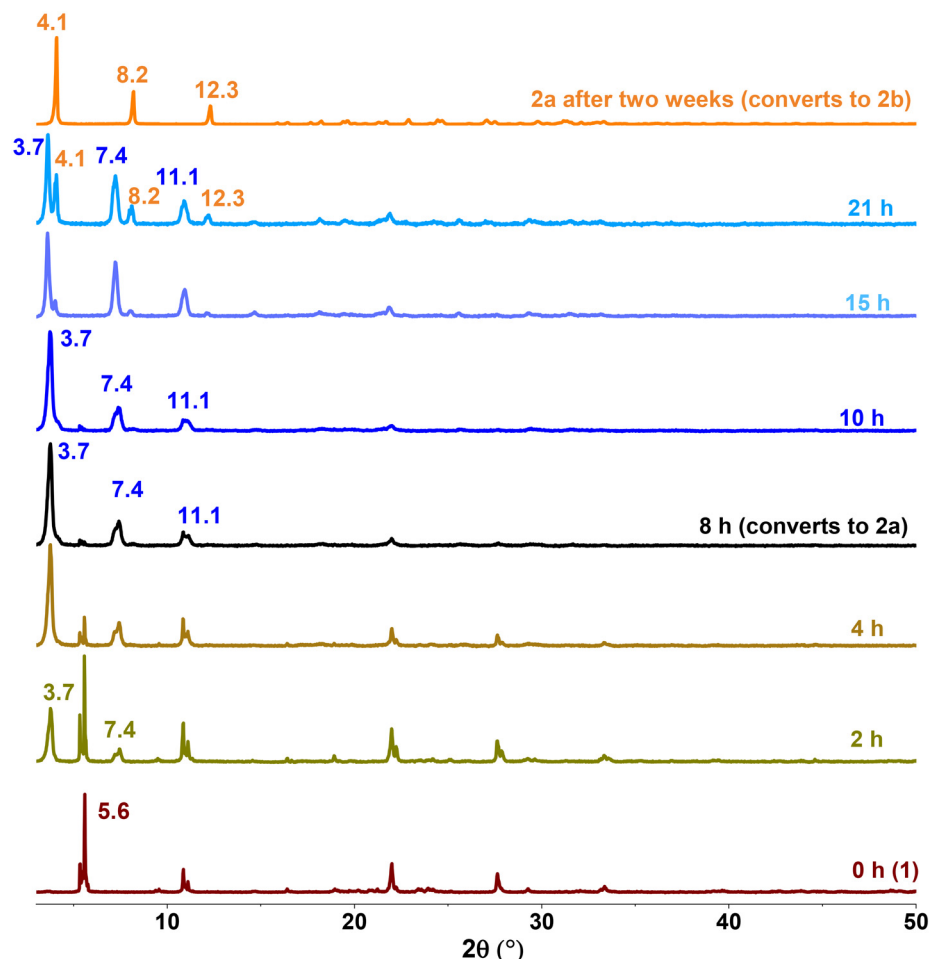


Fig. 5 Structural evolution of  $[^n\text{OctOPO}_3\text{Zn}(\text{H}_2\text{O})]_n$  (**2a** and **2b**) from the freshly prepared  $[^n\text{OctOPO}_3\text{Zn}(\text{DMF})]_n$  (**1**) monitored by powder XRD. Initially, the XRD pattern shows reflections corresponding to **1**, with a 001 reflection peak at  $5.6^\circ$ . As time progresses, new peaks appear corresponding to **2**, having a 001 reflection at  $3.7^\circ$ , while the intensity of reflections due to **1** decreases. After eight hours, the reflections associated with **1** are significantly reduced, indicating that most of it has transformed into **2a**. After fifteen hours, a new pattern began to appear with a 001 reflection peak at  $4.1^\circ$ , corresponding to a decrease in the interlayer distance of **2a** due to the flexible nature of the alkyl chains. Compound **2a** completely transforms to **2b** in two weeks, exhibiting a decreased  $d$ -spacing.

same chemical composition. Furthermore, **2b** was heated at  $50^\circ\text{C}$  under vacuum for 20 hours, resulting in its conversion back to **2a**, as evident by the powder XRD pattern (Fig. S12†). The similar composition of **2a** and **2b** is further supported by the TGA data collected before and after evacuation, which show nearly identical thermal decomposition profiles (Fig. S13†).

The temperature-dependent structural changes were studied using variable temperature powder XRD for **2b** and **4**. For compound **2b**, the reflection appearing at  $4.1^\circ$  at room temperature shifts to a lower  $2\theta$  value of  $3.7^\circ$  on heating to  $200^\circ\text{C}$ , signifying expansion of the interlayer distance ( $d$ -spacing) (Fig. S15a†), which matches with the interlayer distance of **2a**. However, this phase could not be assigned to **2a** since the coordinated water will be lost at such a high temperature, as evident from the TGA results (Fig. 6a). However, it can be inferred that the alkyl chains have the same orientation as that of **2a**, since water, being a small molecule that is

buried within the structure, has little effect on the interlayer distance, which is predominantly governed by the organization of the alkyl chains. While not widely reported, there are a few examples of layered phosphonates in the literature, such as zinc ethyl phosphonate produced by Mallouk and co-workers<sup>66</sup> and zinc phenyl phosphonate produced by Clearfield and co-workers,<sup>67</sup> where the hydrated and dehydrated phases exhibit similar interlayer spacings. Similarly, variable temperature powder XRD of **4** reveals temperature-dependent phase transformation (Fig. S16a†). The reflection originally appearing at  $4.6^\circ$  shifts to a lower value of  $4.0^\circ$  on heating to  $150^\circ\text{C}$ , indicating an expansion of the interlayer distance from  $19.6\text{ \AA}$  at room temperature to  $22.1\text{ \AA}$  at  $150^\circ\text{C}$ . Further cooling cycles were recorded for these transitions, which show the irreversible nature of these temperature-dependent transitions (Fig. S15b and S16b†). These observations indicate the flexible nature of the alkyl chain in **2a** and **4** and suggest that the layered metal alkyl phosphates can exist in phases having

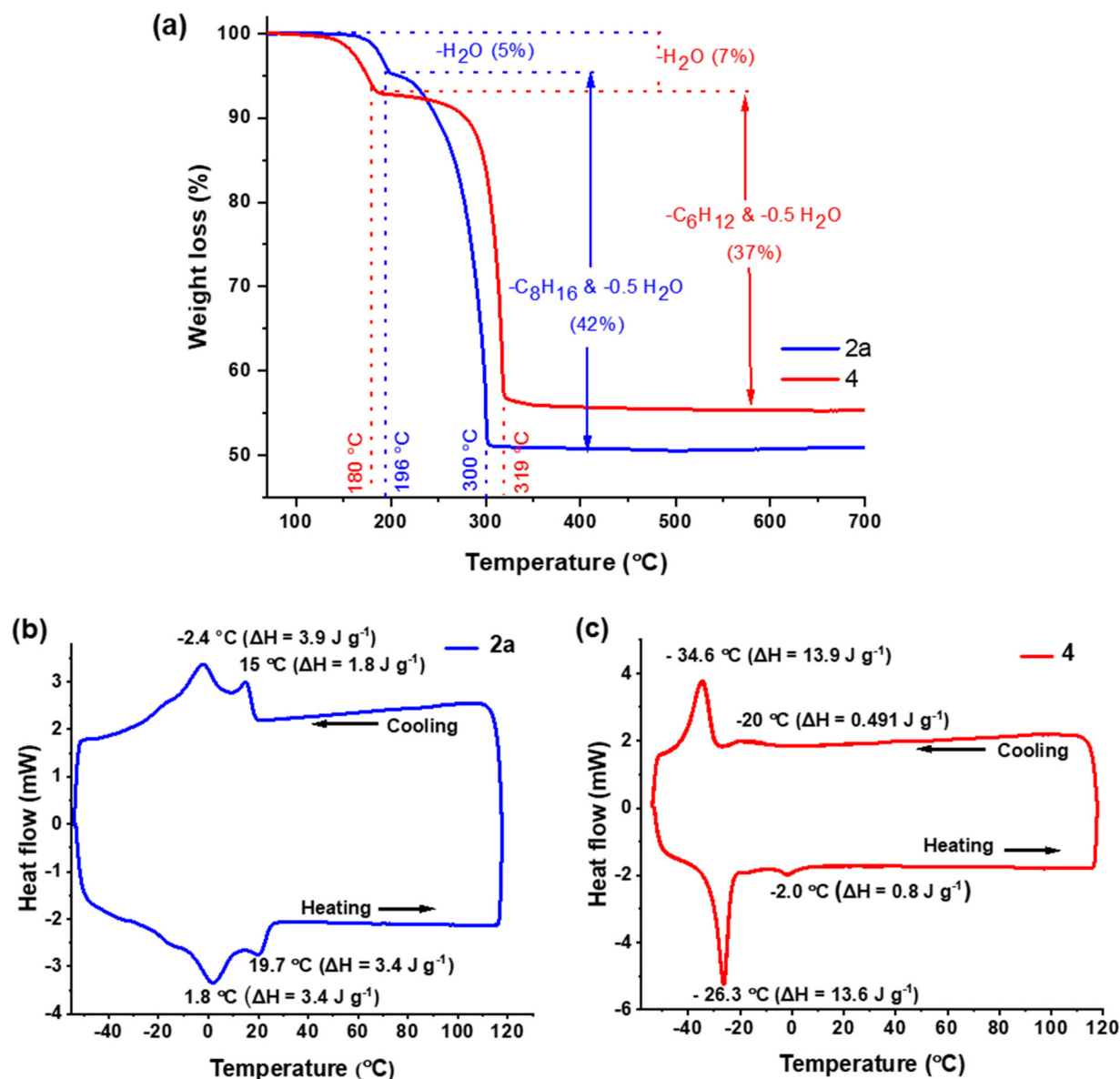


Fig. 6 (a) TGA traces of 2a and 4 recorded under a flow of  $\text{N}_2$  at a heating rate of  $10 \text{ }^\circ\text{C min}^{-1}$ ; (b and c) DSC plots of 2a and 4, respectively, at a scanning rate of  $10 \text{ }^\circ\text{C min}^{-1}$  under an  $\text{N}_2$  atmosphere.

different interlayer distances due to the flexibility (folding and unfolding) of the alkyl chains. This further explains the huge variation in the interlayer spacing observed in the metal alkyl phosphates having the same alkyl chain length, as can be seen in Table S5.†

### 3.5. Thermal studies

Metal alkyl phosphates undergo  $\beta$ -hydride elimination at elevated temperatures, leading to the formation of metal phosphates at comparatively lower temperatures.<sup>68</sup> We have investigated the thermal decomposition of compounds 1–4 using TGA under a nitrogen atmosphere at a heating rate of  $10 \text{ }^\circ\text{C min}^{-1}$ . TGA of 1 and 3 shows initial weight loss of approximately 21.0% and 24.3%, respectively, occurring at around

120 °C (Fig. S17†), consistent with the loss of coordinated DMF molecules. For compound 3, the observed weight loss slightly exceeds the calculated value of 23.0% for the loss of DMF molecules. This minor discrepancy is attributed to the presence of surface-adsorbed water, as also indicated by a slight weight loss beginning at room temperature. Despite this, the first major weight loss event in both compounds occurs near 120 °C, confirming that the majority of the mass loss is due to DMF molecules. Subsequent weight loss of 35% for 1 and 29% for 3 at 300 °C corresponds to the loss of alkene and water molecules *via* condensation of two P–OH groups, respectively. Compounds 2a and 4 exhibit similar decomposition patterns in TGA (Fig. 6a). An initial weight loss of 5% and 7% at 200 °C for 2a and 4, respectively, indicates the loss

of coordinated water molecules. This was followed by another weight loss of 42% for **2a** and 37% for **4** at 300 °C, attributed to  $\beta$ -H elimination of the alkyl chains and subsequent water release *via* condensation of phosphate hydroxyl groups.

To investigate the structural changes associated with decomposition of zinc alkyl phosphates and the formation of ceramic zinc phosphates, we conducted variable temperature powder XRD for compound **2b** over a range of temperatures up to 800 °C (Fig. S14†). Upon heating at 300 °C, **2b** underwent conversion to an amorphous phase as revealed in the powder XRD profile. This is attributed to the loss of the octyl groups, which can also be confirmed by the weight loss at 300 °C observed in the thermogram (Fig. S13†). The amorphous phase remained until 550 °C, above which a crystalline phase started to appear with complete crystallization occurring at 800 °C.

It has been earlier shown that the temperature-dependent structural transformations in metal complexes are facilitated by the inherent flexibility of their alkyl chains.<sup>44,51</sup> Recently, we have shown that these transitions are associated with the folding of alkyl chains, resulting in the change of the crystal system as showcased in  $[(\text{phen})\text{Ca}(\text{ehpH})_2]_n$ .<sup>51</sup> Due to the presence of flexible alkyl chains in **2a** and **4**, these compounds are expected to show temperature-dependent phase transitions. These transitions can be observed by DSC measurements in the temperature range of -50 °C to 115 °C under a nitrogen atmosphere. The heat flow *versus* temperature plot of **2a** reveals two low-enthalpy exothermic transitions at 15 °C ( $\Delta H = 1.8 \text{ J g}^{-1}$ ) and -2.4 °C ( $\Delta H = 3.9 \text{ J g}^{-1}$ ) during the cooling cycle (Fig. 6b). Corresponding endothermic peaks were observed upon heating at 1.8 °C ( $\Delta H = 3.4 \text{ J g}^{-1}$ ) and 19.7 °C ( $\Delta H = 1.8 \text{ J g}^{-1}$ ). The low-enthalpy transition at 19.7 °C explains the observed room temperature structural changes in **2a**. In the case of **4**, the heat flow *vs.* temperature plot reveals a low-enthalpy exothermic transition at -20 °C ( $\Delta H = 0.491 \text{ J g}^{-1}$ )

and a high-enthalpy exothermic transition at -34.8 °C ( $\Delta H = 13.9 \text{ J g}^{-1}$ ) (Fig. 6c). Upon heating, corresponding endothermic peaks are observed at -26.3 °C ( $\Delta H = 13.6 \text{ J g}^{-1}$ ) and -2.0 °C ( $\Delta H = 0.8 \text{ J g}^{-1}$ ).

### 3.6. Solid-state thermolysis

Bulk thermolysis of compounds **2a** and **4** at 800 °C for 24 h in air results in highly crystalline products **2-800 °C** and **4-800 °C**, respectively. The powder XRD plots of **2a-800 °C** and **4-800 °C** are identical, indicating that thermolysis of **2a** and **4** gives rise to the same ceramic metal phosphate product (Fig. 7a). The observed powder XRD patterns do not match with any of the earlier reported zinc phosphate or pyrophosphate phases. However, monoalkyl phosphate-based metal complexes are known to undergo thermal decomposition to form a metal pyrophosphate product.<sup>26,27</sup> ICP-AES reveals the ratio of Zn and P in **2a-800 °C** and **4-800 °C** to be 1:0.915 and 1:1.32, respectively, consistent with the stoichiometric range for zinc pyrophosphate.

The infrared spectra of **2a-800 °C** and **4-800 °C** show similar profiles, with absorption bands characteristic of  $\text{Zn}_2\text{P}_2\text{O}_7$  (Fig. S18†).<sup>69,70</sup> The FT-IR absorption bands at 1180, 1126 and 1075  $\text{cm}^{-1}$  correspond to the asymmetric stretching of the  $\text{PO}_3^{2-}$  unit ( $\nu_{\text{as}}(\text{PO}_3^{2-})$ ), whereas the absorption bands at 1043 and 1010  $\text{cm}^{-1}$  are assigned to its symmetric stretching ( $\nu_{\text{s}}(\text{PO}_3^{2-})$ ). The absorption bands appearing at 951  $\text{cm}^{-1}$  ( $\nu_{\text{as}}(\text{P-O-P})$ ) and 754  $\text{cm}^{-1}$  ( $\nu_{\text{s}}(\text{P-O-P})$ ) signifies the presence of the P-O-P bond. The band appearing at 540  $\text{cm}^{-1}$  is assigned to the O-P-O bending vibration ( $\delta(\text{P-O})$ ) of the  $\text{P}_2\text{O}_7^{2-}$  unit.<sup>69,70</sup> The Raman spectra of **2a-800 °C** and **4-800 °C** further complement the formation of the pyrophosphate phase. The Raman peaks at 1180  $\text{cm}^{-1}$  and 1137  $\text{cm}^{-1}$  correspond to  $\nu_{\text{as}}(\text{PO}_3^{2-})$ , while peaks at 1069 and 1005  $\text{cm}^{-1}$  are attributed to  $\nu_{\text{s}}(\text{PO}_3)$  (Fig. 7b). The peak observed at 950  $\text{cm}^{-1}$  corresponds to  $\nu_{\text{as}}(\text{P-O-P})$  stretching, whereas the peak at 777  $\text{cm}^{-1}$

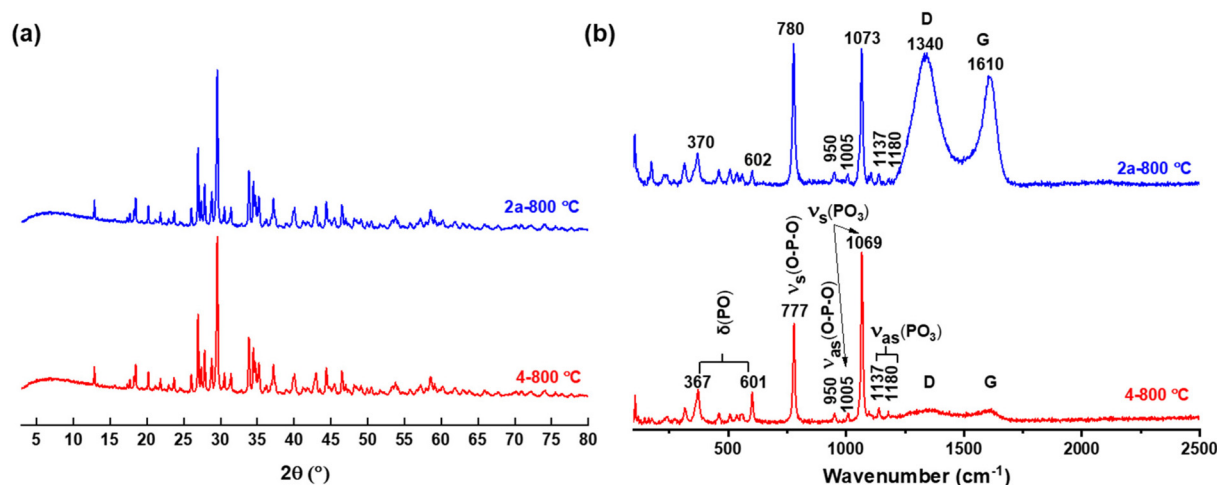
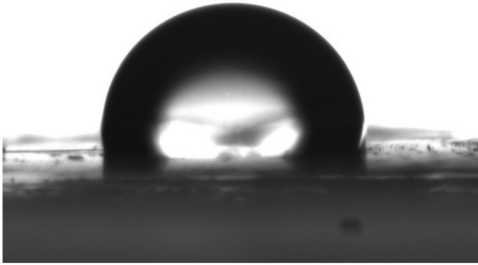
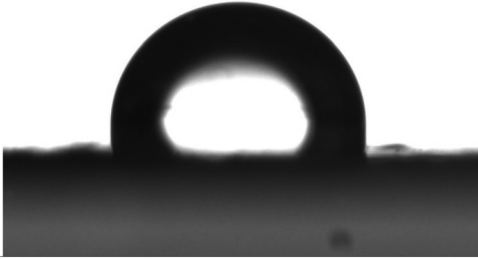


Fig. 7 (a) Powder XRD patterns of bulk thermolysis products **2a-800 °C** and **4-800 °C** recorded upon heating **2a** and **4** at 800 °C for 24 h showing the formation of a new phase of zinc phosphate. (b) Raman spectra of **2a-800 °C** and **4-800 °C** (632 nm laser) showing the presence of residual carbon in **2a-800 °C**.

Table 2 Contact angles of **2a** and **4**

Sample	Image	Contact angle (°)
<b>2a</b>		100.5 (±0.2)
<b>4</b>		98.8 (±0.2)

is assigned to  $\nu_s(\text{P-O-P})$ . Additionally, the peaks at 601 and 367  $\text{cm}^{-1}$  correspond to the O-P-O bending vibration ( $\delta(\text{PO})$ ) of the  $\text{P}_2\text{O}_7^{2-}$  unit.<sup>71,72</sup> Furthermore, the additional peaks observed in the Raman spectra at 1340 and 1610  $\text{cm}^{-1}$  correspond to the D and G bands of carbon, indicating the presence of residual carbon.<sup>51,73</sup> The intensity of peaks due to carbon in the Raman spectrum for **4**-800 °C is less relative to the peak intensity for **2a**-800 °C, suggesting a lower residual carbon content in **4** after thermal treatment. The presence of residual carbon in the pyrolyzed products is further confirmed *via* SEM-EDS analysis (Fig. S19 and S20†). The single-pulse  $^{31}\text{P}$  NMR spectra of **2a**-800 °C and **4**-800 °C show peaks at  $\delta$  5.78,  $\delta$  1.36 ppm, and at  $\delta$  5.75,  $\delta$  1.44 ppm, respectively, indicating the presence of two non-equivalent phosphate centres in the structure (Fig. S21†).

### 3.7. Contact angle measurements

Corrosion protection materials are coated with functional groups bearing alkyl chains, owing to their hydrophobic nature.<sup>52,74,75</sup> The hydrophobicity of alkyl chains prevents the interaction of water molecules with metal surfaces and hence protects them from corrosion.<sup>76</sup> Since the structures of **2a** and **4** feature alkyl chains, they are expected to show hydrophobic behaviour; hence, contact angle measurements were conducted to examine the surface interaction of **2a** and **4** with water droplets. Pellets of **2a** and **4** were made by using a hydraulic press and subjected to static contact angle measurements, resulting in observed angles of 100.5° (±0.2) for **2a** and 98.8° (±0.2) for **4** (Table 2). These values indicate hydrophobicity and suggest that, although the coordination polymer is hydrated, the surface is enriched with alkyl chains that either extend outward or are oriented near the interface. This surface composition effectively imparts hydrophobic character to the

material by minimizing water-surface interactions. These studies imply that **2a** and **4** could serve as effective hydrophobic coating materials.<sup>77</sup>

## 4. Conclusions

Zinc phosphate coordination polymers  $[(\text{RO})\text{PO}_3\text{Zn}(\text{DMF})]_n$  ( $\text{R} = n\text{-octyl}$  (**1**) and  $n\text{-hexyl}$  (**3**)) and  $[(\text{RO})\text{PO}_3\text{Zn}(\text{H}_2\text{O})]_n$  ( $\text{R} = n\text{-octyl}$  (**2a**) and  $n\text{-hexyl}$  (**4**)) have been synthesized by respective facile reactions between zinc nitrate hexahydrate and  $n\text{-octyl}$  phosphate and  $n\text{-hexyl}$  phosphate by mixing the reagents. Single-crystal X-ray diffraction studies of **1** and **3** show the formation of 1D railroad-type or tape-like polymeric structures. These 1D polymeric chains arrange themselves to form arrays having interdigitated alkyl chains with an inter-polymer distance of 15.3 Å and 13.4 Å for **1** and **3**, respectively. Interestingly, DMF-coordinated polymers **1** and **3** undergo a facile transformation where the DMF molecules are exchanged with water molecules, leading to the formation of **2a** and **4**, respectively. Powder XRD studies of **2a** and **4** indicate the formation of 2D layered structures with interlayer distances of 23.8 Å and 19.6 Å for **2a** and **4**, respectively, indicating structural expansion as a result of DMF-water exchange. The flexible nature of long alkyl chains in **2a** ( $d = 23.8$  Å) leads to the contraction of interlayer spacing over time to form **2b** ( $d = 21.6$  Å). The presence of structural transformations at lower temperatures has been confirmed by DSC studies. Thermal decomposition studies reveal that **2a** and **4** transition to an amorphous phase at 300 °C, which then transforms to a crystalline phase having an approximate Zn to P ratio of 1 : 1 at 800 °C. Furthermore, contact angle measurements indicate the hydrophobic nature of 2D layered zinc alkyl phosphates.



In conclusion, this work highlights the role of alkyl chains and solvent coordination for shaping the layered structures. The transformation from 1D to 2D structures upon replacement of coordinated DMF with water demonstrates the role of solvent molecules in directing the dimensionality of the framework assembly. Thermal and contact angle studies reveal the utility of zinc alkyl phosphates as single-source precursors for ceramic phosphates and hydrophobic materials, underscoring the potential of these systems in designing functional materials with tailored structural properties.

## Conflicts of interest

The authors declare no conflict of interest.

## Data availability

The data supporting this article have been included as part of the ESI.† Crystallographic data have been deposited at the CCDC under deposition numbers 2350478 (for **1**) and 2350479 (for **3**).†

## Acknowledgements

This work was supported by SERB, New Delhi (CRG/2022/002406 & SB/S2/JCB-85/2014). Harsha Arya acknowledges CSIR, New Delhi, for the award of a fellowship. The authors thank the Sophisticated Analytical Instrument Facility (SAIF) at IIT Bombay and the IoE-funded central facilities (IOE funding) for providing access to equipment used in this work.

## References

- Y. He, X. Shen and Y. Zhang, *ACS Appl. Nano Mater.*, 2024, **7**, 27907–27939.
- L. Peng, Y. Zhu, D. Chen, R. S. Ruoff and G. Yu, *Adv. Energy Mater.*, 2016, **6**, 1600025.
- H. Liao, Y. Jiang, X. Wei, X. Zhao, W. Lai, N. An, Y. Ma, S. Dai and Z. Hou, *ACS Sustainable Chem. Eng.*, 2024, **12**, 2632–2645.
- S. Yadav, J. Das, S. P. Chaurasia, L. Singh and P. Rekha, *Chem. Eng. Sci.*, 2024, **285**, 119628.
- T. Dutta, N. Yadav, Y. Wu, G. J. Cheng, X. Liang, S. Ramakrishna, A. Sbair, R. Gupta, A. Mondal and Z. Hongyu, *Nano Mater. Sci.*, 2024, **6**, 1–23.
- J. Zhou, C. Wang, X. Zhang, L. Jiang and R. Wu, *Mater. Sci. Eng., R*, 2024, **161**, 100872.
- M. R. A. Karim, W. Shehzad, K. I. Khan, E. U. Haq and Y. Haroon, *J. Electrochem. Sci. Technol.*, 2024, **15**, 321–344.
- R. Lin and Y. Ding, *Materials*, 2013, **6**, 217–243.
- M. Beiro, A. Collazo, M. Izquierdo, X. Nóvoa and C. Pérez, *Prog. Org. Coat.*, 2003, **46**, 97–106.
- J. Juárez-Batalla, A. Meza-Rocha, I. Camarillo and U. Caldiño, *Opt. Mater.*, 2016, **58**, 406–411.
- N. Attar, L. E. Tam and D. McComb, *J. Prosthet. Dent.*, 2003, **89**, 127–134.
- P. Pascuta, G. Borodi, A. Popa, V. Dan and E. Culea, *Mater. Chem. Phys.*, 2010, **123**, 767–771.
- I. R. Sayed, A. M. Farhan, A. A. AlHammadi, M. I. El-Sayed, I. M. Abd El-Gaied, A. M. El-Sherbeeney, W. Al Zoubi, Y. G. Ko and M. R. Abukhadra, *J. Mol. Liq.*, 2022, **360**, 119527.
- J. Li, Z. Zheng, Z. Yu, F. She, L. Lai, J. Prabowo, W. Lv, L. Wei and Y. Chen, *J. Mater. Chem. A*, 2023, **11**, 3051–3059.
- S. Xia, Q. Luo, J. Liu, X. Yang, J. Lei, J. Shao and X. Tang, *Small*, 2024, **20**, 2310497.
- Q. Jing, M. Zhu, L. Li, X. Ji, H. Duan, H. Chen and M.-H. Lee, *Opt. Mater.*, 2024, **147**, 114620.
- Y. L. Sun, G. X. Liu, Y. L. Lv, L. Ma, W. D. Yao and R. L. Tang, *J. Solid State Chem.*, 2023, **325**, 124171.
- S. Vafaei, S. A. Sadat Shandiz and Z. Piravar, *Biol. Trace Elem. Res.*, 2020, **198**, 109–117.
- X. Hu, X. Song, Y. Yuan, X. Yao, X. Chen, G. Li and S. Li, *J. Mater. Chem. B*, 2023, **11**, 6404–6411.
- P. C. Jhang, N. T. Chuang and S. L. Wang, *Angew. Chem., Int. Ed.*, 2010, **25**, 4296–4300.
- Z. Fu, D. Song, Y. Zeng, S. Liao and J. Dai, *Dalton Trans.*, 2012, **41**, 10910–10912.
- K. M. Zhang, X. L. Zhong, X. Y. Zhou, X. T. Kuang and H. R. Zhao, *Polyhedron*, 2024, **264**, 117258.
- S. Neeraj, S. Natarajan and C. Rao, *Chem. Mater.*, 1999, **11**, 1390–1395.
- J. Fan and B. E. Hanson, *Inorg. Chem.*, 2005, **44**, 6998–7008.
- J. Vallejo, I. R. Salcedo, R. M. Colodrero, A. Cabeza, A. Świtlicka, J. Cano and M. Viciano-Chumillas, *Dalton Trans.*, 2017, **46**, 16570–16579.
- G. A. Bhat, S. Haldar, S. Verma, D. Chakraborty, R. Vaidhyanathan and R. Murugavel, *Angew. Chem.*, 2019, **131**, 17000–17005.
- G. A. Bhat, A. C. Kalita and R. Murugavel, *CrystEngComm*, 2017, **19**, 5390–5401.
- T. Lis, *Acta Crystallogr., Sect. C: Cryst. Struct. Commun.*, 1994, **50**, 181–185.
- Y. Ortiz-Avila, P. R. Rudolf and A. Clearfield, *Inorg. Chem.*, 1989, **28**, 2137–2141.
- P. Bissinger, O. Kumberger and A. Schier, *Chem. Ber.*, 1991, **124**, 509–513.
- S. Verma and R. Murugavel, *Inorg. Chem.*, 2022, **61**, 6807–6818.
- S. Verma and R. Murugavel, *Inorg. Chem.*, 2020, **59**, 13233–13244.
- R. Murugavel and S. Chaudhary, *Chem. – Asian J.*, 2025, e202401177.
- R. Pothiraja, M. Sathiyendiran, R. J. Butcher and R. Murugavel, *Inorg. Chem.*, 2004, **43**, 7585–7587.
- R. Murugavel, M. Sathiyendiran and M. G. Walawalkar, *Inorg. Chem.*, 2001, **40**, 427–434.

- 36 M. Sathiyendiran and R. Murugavel, *Inorg. Chem.*, 2002, **41**, 6404–6411.
- 37 R. Pothiraja, M. Sathiyendiran, R. J. Butcher and R. Murugavel, *Inorg. Chem.*, 2005, **44**, 6314–6323.
- 38 C. G. Lugmair, T. D. Tilley and A. L. Rheingold, *Chem. Mater.*, 1997, **9**, 339–348.
- 39 C. G. Lugmair, T. D. Tilley and A. L. Rheingold, *Chem. Mater.*, 1999, **11**, 1615–1620.
- 40 K. L. Fajdala and T. D. Tilley, *J. Am. Chem. Soc.*, 2001, **123**, 10133–10134.
- 41 K. M. Van Allsburg, E. Anzenberg, W. S. Drisdell, J. Yano and T. D. Tilley, *Chem. – Eur. J.*, 2015, **21**, 4646–4654.
- 42 S. Chaudhary and R. Murugavel, *Chem. Mater.*, 2024, **36**, 6475–6488.
- 43 G. A. Bhat, S. Verma, A. Rajendran and R. Murugavel, *Inorg. Chem.*, 2018, **57**, 7644–7654.
- 44 K. Omoto, S. Aoyama, T. Galica, E. Nishibori, S. Katao, K. Yasuhara and G. Rapenne, *Dalton Trans.*, 2022, **51**, 17967–17972.
- 45 T. Minami, H. Sato and S. Matsumoto, *CrystEngComm*, 2018, **20**, 2644–2647.
- 46 Z. S. Yao, M. Mito, T. Kamachi, Y. Shiota, K. Yoshizawa, N. Azuma, Y. Miyazaki, K. Takahashi, K. Zhang and T. Nakanishi, *Nat. Chem.*, 2014, **6**, 1079–1083.
- 47 S. Q. Su, T. Kamachi, Z. S. Yao, Y. G. Huang, Y. Shiota, K. Yoshizawa, N. Azuma, Y. Miyazaki, M. Nakano and G. Maruta, *Nat. Commun.*, 2015, **6**, 8810.
- 48 S. H. Kang, Y. J. Jin and G. Kwak, *ACS Appl. Polym. Mater.*, 2020, **2**, 2987–2993.
- 49 S. Hayami, K. Kato, Y. Komatsu, A. Fuyuhiko and M. Ohba, *Dalton Trans.*, 2011, **40**, 2167–2169.
- 50 S. Hayami, R. Moriyama, A. Shuto, Y. Maeda, K. Ohta and K. Inoue, *Inorg. Chem.*, 2007, **46**, 7692–7694.
- 51 N. Matharoo, M. G. Walawalkar and R. Murugavel, *Dalton Trans.*, 2023, **52**, 2412–2423.
- 52 X. Gao, S. Liu, H. Lu, F. Gao and H. Ma, *Ind. Eng. Chem. Res.*, 2015, **54**, 1941–1952.
- 53 *CrysAlisPRO*, Oxford Diffraction/Agilent Technol. UK Ltd, Yarnton, Oxford, UK.
- 54 G. M. Sheldrick, *Acta Crystallogr., Sect. C: Struct. Chem.*, 2015, **71**, 3–8.
- 55 O. V. Dolomanov, L. J. Bourhis, R. J. Gildea, J. A. K. Howard and H. Puschmann, *J. Appl. Crystallogr.*, 2009, **42**, 339–341.
- 56 M. Llunell, D. Casanova, J. Cirera, P. Alemany and S. Alvarez, *SHAPE (Version 2.1)*, Universitat de Barcelona, Barcelona, 2013.
- 57 G. A. Bhat and R. Murugavel, *J. Chem. Sci.*, 2020, **132**, 1–9.
- 58 R. A. Coxall, S. G. Harris, D. K. Henderson, S. Parsons, P. A. Tasker and R. E. Winpenny, *J. Chem. Soc., Dalton Trans.*, 2000, 2349–2356.
- 59 G. Cao, V. M. Lynch, J. S. Swinnea and T. E. Mallouk, *Inorg. Chem.*, 1990, **29**, 2112–2117.
- 60 H. Tanaka, T. Watanabe, M. Chikazawa, K. Kandori and T. Ishikawa, *Colloids Surf., A*, 1998, **139**, 341–349.
- 61 H. Tanaka and M. Chikazawa, *J. Mater. Chem.*, 1999, **9**, 2923–2927.
- 62 H. Tanaka, K. Masuda and R. Hino, *J. Colloid Interface Sci.*, 2002, **254**, 331–337.
- 63 G. Cao, H. Lee, V. M. Lynch and T. E. Mallouk, *Solid State Ionics*, 1988, **26**, 63–69.
- 64 G. Cao, H. Lee, V. M. Lynch and T. E. Mallouk, *Inorg. Chem.*, 1988, **27**, 2781–2785.
- 65 A. Kondo, T. Nakagawa, H. Kajiro, A. Chinen, Y. Hattori, F. Okino, T. Ohba, K. Kaneko and H. Kanoh, *Inorg. Chem.*, 2010, **49**, 9247–9252.
- 66 G. Cao and T. E. Mallouk, *Inorg. Chem.*, 1991, **30**, 1434–1438.
- 67 Y. Zhang, K. J. Scott and A. Clearfield, *J. Mater. Chem.*, 1995, **5**, 315–318.
- 68 R. Murugavel, *Emergent Mater.*, 2019, **2**, 273–294.
- 69 M. Crobu, A. Rossi, F. Mangolini and N. D. Spencer, *Anal. Bioanal. Chem.*, 2012, **403**, 1415–1432.
- 70 L. Popović, D. De Waal and J. Boeyens, *J. Raman Spectrosc.*, 2005, **36**, 2–11.
- 71 G. Stranford, R. Condrate Sr and B. C. Cornilsen, *J. Mol. Struct.*, 1981, **73**, 231–234.
- 72 B. Wang, Y. Duan, M. Wei, J. Guo, M. Chao, Q. Gao, Y. Gao, Z. Li, J. Xie and E. Liang, *Results Phys.*, 2024, **61**, 107785.
- 73 M. Pimenta, G. Dresselhaus, M. S. Dresselhaus, L. Cancado, A. Jorio and R. Saito, *Phys. Chem. Chem. Phys.*, 2007, **9**, 1276–1290.
- 74 C. C. Pan, X. Z. Wang, Y. Behnamian, Z. Wu, Z. B. Qin, D. H. Xia and W. B. Hu, *J. Electrochem. Soc.*, 2020, **167**, 161510.
- 75 C. Zhao, X. Gao, H. Lu, R. Yan, C. Wang and H. Ma, *RSC Adv.*, 2015, **5**, 54420–54432.
- 76 C. Verma, M. Quraishi and K. Rhee, *Adv. Colloid Interface Sci.*, 2022, **306**, 102723.
- 77 S. Ananthapadmanabhan, T. K. Rout, S. Chatterjee, T. Dasgupta and S. Parida, *ACS Appl. Mater. Interfaces*, 2023, **15**, 51737–51752.